History effects in the creep of a disordered brittle material

Tero Mäkinen, Jérôme Weiss, David Amitrano, Philippe Roux

History effects in the creep of a disordered brittle material

Tero Mäkinen [1,2,*] Jérôme Weiss,[3] David Amitrano,[3] and Philippe Roux[3]
[1]Department of Applied Physics, Aalto University, P. O. Box 11100, 00076 Aalto, Espoo, Finland
[2]NOMATEN Centre of Excellence, National Centre for Nuclear Research, 05-400 Otwock-Świerk, Poland
[3]Université Grenoble Alpes, CNRS, ISTerre, 38000 Grenoble, France

(Received 24 June 2022; revised 1 November 2022; accepted 7 March 2023; published 16 March 2023)

We study the creep behavior of a disordered brittle material (concrete) under successive loading steps, using acoustic emission and ultrasonic sensing to track internal damage. The primary creep rate is observed to follow a (Omori-type) power-law decay in the strain rate, the number of acoustic emission events, as well as the amplitudes of the ultrasonic beams, supporting a brittle-creep mechanism. The distribution of acoustic emission event energies is observed to have a scale-free power-law distribution instead of a truncated one expected for a system approaching a critical point at failure. The main outcome is, however, the discovery of unexpected history effects that make the material less prone to creep when it has been previously deformed and damaged under primary creep. With the help of a progressive damage model implementing thermal activation, we interpret this as an aging-under-stress phenomenon: During an initial creep step at relatively low applied stress, the easy-to-damage sites are exhausted first, depleting the excitation spectrum at low stress gap values. Consequently on reloading, although previously damaged, the primary creep restarts but the material creeps (and damages) less than it would under the same stress but without precreeping. Besides shedding a new light on the fundamental physics of creep of disordered brittle materials, this has important practical consequences in the interpretation of some experimental procedures, such as stress-stepping experiments.

DOI: 10.1103/PhysRevMaterials.7.033602

I. INTRODUCTION

The failure of materials is naturally important for practical applications but also for the fundamental physics involved. In everyday applications, such as in structural materials, the loads are often static, leading to time-dependent deformation—creep—and possibly failure. Understanding this type of deformation is crucial in determining the life expectancy of an aging concrete infrastructure. Such circumstances can be mimicked by imposing a loading history on a sample in laboratory conditions—with constant loading.

Creep behavior of materials is usually divided into distinct phases. The first phase, primary creep, is characterized by a power-law decrease in the strain rate, $\dot{\epsilon} \propto t^{-p}$, where the exponent p is reported [1] to range between 0.4 and 1 (the large variation linked, e.g., to the role of elastic stress redistribution [2]). Andrade historically reported an exponent $p = 2/3$ for metal wires [3], defining the so-called Andrade's creep, while $p = 1$ defines logarithmic creep [$\epsilon \propto \log(t)$] [4]. After primary creep one might enter secondary creep, where the strain rate reaches its minimum value, $\dot{\epsilon}_m$, and stays constant. Finally, the material fails due to a rapid increase in the strain rate, called tertiary creep [5–8]. A classical goal is to determine a creep law of the form $\dot{\epsilon}_m = A\sigma^n \exp(-E/k_B T)$, where σ is the stress, the exponent n is assumed to be linked to an underlying microscopic mechanism, T is the temperature, k_B is the Boltzmann's constant, E is a stress-independent (material-dependent) activation energy, and A is a material constant [9]. In this empirical law, the Arrhenius term expresses the thermally activated nature of creep.

In practice, a stress-stepping procedure is often used for creep testing [10–12] where the sample is first loaded to a stress level for a period of time to study the creep rate and then successively loaded to higher stress levels. This is a cost-effective testing method, as multiple stresses can be tested on the same specimen at a given temperature and sample-to-sample variation in heterogeneous materials can be eliminated. The goal is to determine the creep law of the material, assuming that the minimum strain rate $\dot{\epsilon}_m$ is attained at the end of each step. However, a question naturally arises: Are there history effects in this process, i.e., are the previous creep steps affecting the current one? In the context of dislocation-driven creep in metals, such a possibility was already hinted at by Cottrell [13], who argued that the creep rate in the latter creep steps would be slower as some of the easy-to-deform sites have already been "exhausted" in the initial creep steps. Additionally, in the creep of nonbrittle materials such as metals [14–16] and plastics [17,18] the concepts of strain and time hardening have been discussed in the context of these type of history effects.

In this work we show, from experimental observations of the global strain, acoustic emission and ultrasonic sensing on an emblematic quasibrittle heterogeneous material—concrete—that creep deformation and damage are indeed characterized by history effects leading to unexpected relations between the applied stress and the strain rate. By simulating a simple progressive damage model, we show that

*Corresponding author: tero.j.makinen@aalto.fi

this effect is due to an exhaustion mechanism—a form of *aging-under-stress*—that can make a material, previously deformed and damaged during a primary creep stage, less prone to further deform later under a *larger* stress. These results shed new light on the fundamental physics of creep and might challenge the interpretation of some experimental results, e.g., those based on stress stepping.

The phenomenological power-law decrease of $\dot{\epsilon}$ during primary creep has been observed for a wide range of materials, including metals [3], paper [7], colloidal glasses [19], gels [6,20,21], ice [22], or rocks [10,23]. In various crystalline materials, primary creep mechanisms have been discussed in terms of dislocation interactions [24–27]. In rocks, it has been proposed that primary creep results from the cumulative effect of microfracturing/damage events, defining brittle creep [23,28]. We have chosen concrete for testing, a disordered material of obvious interest in civil engineering. The microscopic origins of concrete creep are still partly unknown [29]. They are usually understood to relate to the nanoscale rearrangements of calcium-silicate-hydrates (primary component of the cement paste) [30–33] or to the migration of adsorbed water in the micro- and nanoporosities [29,31–33] and modelled using viscoelastic approaches [34–39].

Here we, however, take another viewpoint, and later confirm it, of brittle creep [23] where creep results from microcracking. These microcracking events can be indirectly observed as crackling noise [40]. A popular method for observing this crackling noise is acoustic emission (AE) monitoring, which has been used in detecting avalanches in compression of different materials, e.g., porous brittle materials [41], rocks [42,43], solid foams [44,45], and wood [46]. Microcracking avalanches have been studied under monotonic loading of concrete (constant stress-rate) using AE [47,48] and the avalanche energy statistics have shown a scale-free power-law distribution with an upper cutoff, $p(E_{\mathrm{AE}}) \propto E_{\mathrm{AE}}^{-\beta} \exp(-E_{\mathrm{AE}}/E_0)$. When approaching the critical failure stress, the cutoff E_0 diverges, and this critical transition has been mapped to the universality class of depinning [49–51]. We show here that the damage avalanche statistics during primary brittle creep are instead characterized by robust power-law distributions without a cutoff, shining light on fundamental differences between athermal (monotonic loading) and creep (thermally activated) deformation of disordered materials.

II. EXPERIMENTS

The material studied was laboratory-size samples of concrete with two different microstructures, one with medium size aggregates (denoted by M) and one with coarse aggregates (denoted by C). For details on sample preparation and properties, see Appendix A.

To study the effect of increasing load on the same sample, the creep loading was done under uniaxial compression in successive creep steps at room temperature. This means doing a steep ramp of constant stress rate to a stress level σ_1, keeping the stress constant for time T_1, and then doing a second ramp to stress σ_2, keeping the stress constant for time T_2, and so forth. This was done until sample failure which, for the experiments presented here, happened during one of the ramps, defining also the failure stress of the sample σ_c.

The initial loading ramp (as well as the stress increases between stress steps) was performed at a constant force rate of 100 N/s, corresponding to a stress rate of roughly 0.1 MPa/s. The load and axial displacements of the piston were monitored at a 10-Hz frequency. The sample axial displacement was determined by subtracting the known elastic deformation of the loading frame from the measured axial displacement [52].

Additionally, the AE in the sample was monitored using two piezoelectric sensors, yielding a catalog of acoustic event energies E_{AE}. The sample was simultaneously monitored with ultrasonic sensing [53] (measurements at 6-min intervals, which are removed from the AE data) using two arrays of ultrasonic transducers to follow the evolution of the attenuation of direct (ballistic) elastic waves within the material, a way to probe internal damage of the sample. See Appendix A for full experimental details.

III. MODEL

To explore the behavior computationally, we used a finite-element-based progressive damage model (the athermal version has been extensively detailed elsewhere [54–56]). Here the time-dependent, thermally activated creep process is introduced using a kinetic Monte Carlo (KMC) algorithm [57] to allow the damaging of element i with a rate $\nu_i(\sigma, T) = \nu_0 \exp(-E_i/k_B T)$, where ν_0 is an attempt frequency, and the local activation energy is written $E_i = V_a \Delta\sigma_i$ with V_a a constant activation volume and $\Delta\sigma_i$ the Coulomb stress gap between the local stress state and the failure envelope, i.e., the how far the element is from being damaged. Each damage event corresponds to a 10% loss of the elastic modulus of the element. After the element is damaged, the time step for the KMC algorithm is drawn from an exponential distribution with a mean corresponding to the reciprocal of the sum of the jump rates of all the elements in the sample.

The simulation protocol used here, under uniaxial compression, corresponds to initially loading the sample to 80% of the maximum stress (determined from monotonically and athermally loading the same microstructure until failure) for 700 s and then increasing the stress to either 85% or 95% of the maximum stress for additional 700 s. The simulations are averaged over 100 realizations of the microstructure. For full simulation details see Appendix B.

IV. RESULTS

Here for the sake of clarity, we have focused on a single representative experiment and a reference experiment (see Appendix F for additional experiments showing fully consistent results). Looking at the accumulated strain from the beginning of each step [Fig. 1(a)], we observe the strain rate decreasing with time. By assuming an Andrade-like law [3] to hold and avoiding the divergence at the start of the creep step ($t = t_r$) by introducing a time constant c, one arrives at the equation

$$\dot{\epsilon} = \frac{K}{(t - t_r + c)^p}, \tag{1}$$

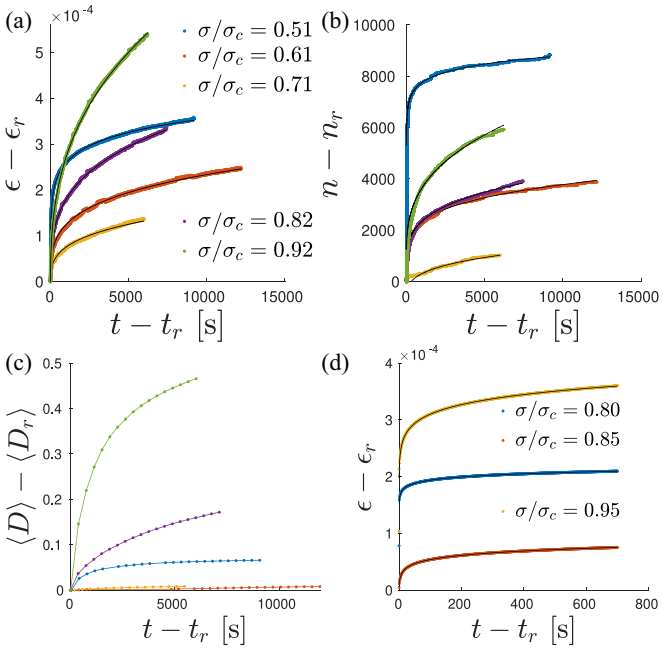

FIG. 1. (a) Strain ϵ accumulated after the start of each creep step as a function of time t after the start of the step at t_r. (b) Same as (a) for the number of acoustic events n. (c) Same as (a) for the damage parameter D, averaged over the sample. (d) Same as (a) for the simulations. The black lines represent fits according to Eq. (1).

where $\dot{\epsilon}$ is the strain rate, $t - t_r$ the time from the start of the creep at t_r, p an exponent, and K a prefactor. The time constant was found to be small compared to the step duration and not to vary significantly between different steps and experiments, so a constant $c = 1$ s was set. By integrating Eq. (1) and fitting to the strain data [black lines in Fig. 1(a)] we see that it works extremely well (see Appendix C for a detailed goodness-of-fit analysis). We observe a slight decrease in the exponent p with increasing applied stress (see Appendix D), consistently with former observations [1,13] and recent simulations [2].

On the same fits one would expect the prefactor K to have a power-law dependency on the applied stress $K \propto \sigma^m$ [1] or at least a monotonically increasing one. This is complicated here by the slight change in the p value; nevertheless, one would expect the creep rate to increase with increasing stress. This is clearly not the case in our experiments [Fig. 1(a)]: After the initial creep step at $0.51 \times \sigma_c$, primary creep is comparatively slower during the following stress steps ($0.61 \times \sigma_c$ to $0.82 \times \sigma_c$)—until one reaches the stress $0.92 \times \sigma_c$ at which creep dynamics finally surpasses that of the initial stress step.

If creep results from the cumulative effect of microcracking events [23], then one would expect the strain rate to be directly proportional to the acoustic event rate $\dot{n}$, which would have therefore an Omori-type relation,

$$\dot{n} = \frac{K'}{(t - t_r + c)^p}, \tag{2}$$

where K' is a different prefactor. Indeed, we see this clear decrease in the event rate in the experimental data [Fig. 1(b)]. To check the proportionality $\dot{\epsilon} \propto \dot{n}$, we take the fits from Fig. 1(a) and apply a linear transformation to yield fits for the number of acoustic events [black lines in Fig. 1(b)]. The agreement observed strongly argues for the brittle creep hypothesis for concrete. It also implicitly suggests that the shape of the distribution of microcrack sizes, i.e., of AE energies, does not evolve during primary creep or from one loading step to another (see below).

We also measured the amplitudes A of the direct waves between transmitting and receiving ultrasonic transducers (from each source to each receiver, see Appendix A for details), normalized by their amplitude at the beginning of the first creep step A_0, and argue that a decrease in this amplitude (attenuation) reflects a damaging process. The damage parameter, averaged over all the beams (over the whole sample), is therefore defined as

$$\langle D \rangle = \left\langle \frac{A_0 - A}{A_0} \right\rangle. \tag{3}$$

The evolution of this damage parameter [Fig. 1(c)] is very similar to the evolution of the strain or the number of events: It grows with time with a decreasing rate, and in the stress steps directly after the initial $0.51 \times \sigma_c$ one, the damage accumulation is slower. This confirms the brittle creep mechanism as well as the associated history effects.

The simulation results agree remarkably well with these experimental findings: The strains follow Eq. (1) [black lines in Fig. 1(d)], and the history effect on the creep rate is evident when the stress of the second creep step is small enough ($0.85 \times \sigma_c$) while with a high-enough stress ($0.95 \times \sigma_c$) the initial rate (at $0.80 \times \sigma_c$) is surpassed, as observed in Fig. 1(a). Similarly to the experiments, the exponent p of Eq. (1) decreases with increasing stress (see Appendix D for details).

The model allows us to ascribe these history effects on creep deformation to a aging-under-stress mechanism. We do this by examining the excitation spectra [58–61], i.e., the Coulomb stress gap distribution (element's distance to being damaged, see Appendix B for details). The simulations start with a uniform cohesion distribution mimicking microstructural disorder, leading to a uniform stress gap distribution. However, this distribution is rapidly depleted toward the small stress gaps as primary creep proceeds (Fig. 2), as the easy-to-damage sites are exhausted. This leads to a slowing down of the creep rate in the second step at $0.85 \times \sigma_c$, for which the lower cut-off of the stress gap distribution does not almost evolve on reloading. Increasing further the applied stress to $0.95 \times \sigma_c$ counterbalances this aging effect and the stress gap distribution significantly narrows at both ends during creep. Coupled with a general softening of the material as damage accumulates, this makes the creep dynamics finally surpass the one of the initial stress step.

In addition to the number of acoustic events, one can take a look at the distribution of their energies. Plotting their cumulative distribution $P(\geqslant E_{\mathrm{AE}})$ (Fig. 3) one can see a power-law type distribution spanning several decades in energy. For (athermal) monotonic loading of concrete, this distribution was found to follow a truncated power law where the cutoff scale E_0 diverges as the sample approaches failure, signing a divergence of the correlation length and a critical transition [47]. Creep fundamentally differs in this respect, as we do not observe such a cutoff, even under stresses far from the monotonic failure stress σ_c of the material and/or during

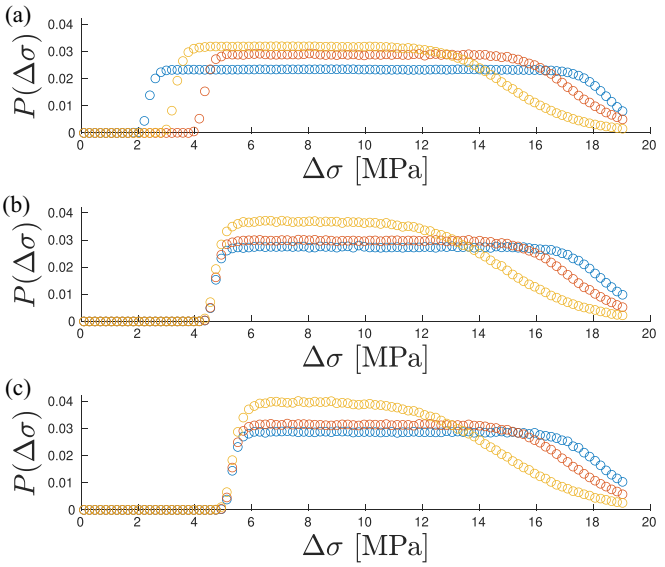

FIG. 2. The distribution of the Coulomb stress gaps $\Delta\sigma$ at (a) $t - t_r = 0.35$ s, (b) $t - t_r = 10$ s, and (c) $t - t_r = 700$ s in the simulations. Blue dots correspond to the initial step at $0.80 \times \sigma_c$, red dots to the step at $0.85 \times \sigma_c$, and yellow ones to $0.95 \times \sigma_c$.

primary creep, i.e., far from the creep failure time. Instead, the distributions follow a pure power-law $p(E_{\mathrm{AE}}) \propto E_{\mathrm{AE}}^{-\beta}$. Note that a truncated power law cannot be statistically excluded (see Appendix E for details on the statistical analysis) for the onset of primary creep during the first loading steps of two experiments, though associated to a large E_0.

By obtaining a maximum likelihood estimate for the exponent β we see [Fig. 3(b)] that it does not change between experiments or creep steps. The observed value of $\beta = 1.47 \pm 0.04$ is very close to the mean-field value of $\beta = 3/2$.

These unexpected history effects are confirmed by other experiments with steps of increasing load (see Appendix F), as well as by a reference experiment with a large number of successive creep steps under the same applied stress, separated by unloading-reloading (Fig. 4). We see [Fig. 4(a)], as expected, a decrease in the creep rate as the number of steps n_{steps} increases, but after a few steps the effect seems to saturate and the difference in the creep rate between steps is very small. We note that the creep rate in the beginning

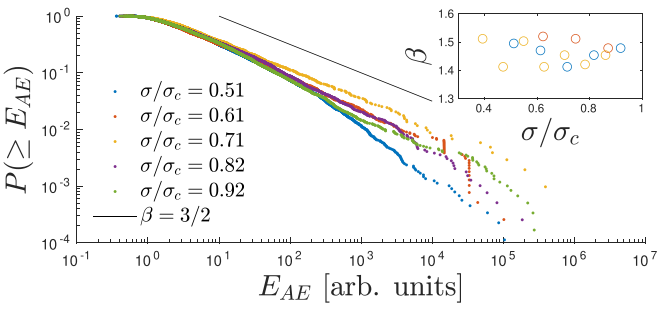

FIG. 3. The cumulative distribution of AE event energies E_{AE} for each of the creep steps in one experiment. The inset shows the values of the power-law exponent β obtained through a maximum likelihood estimation for all experiments.

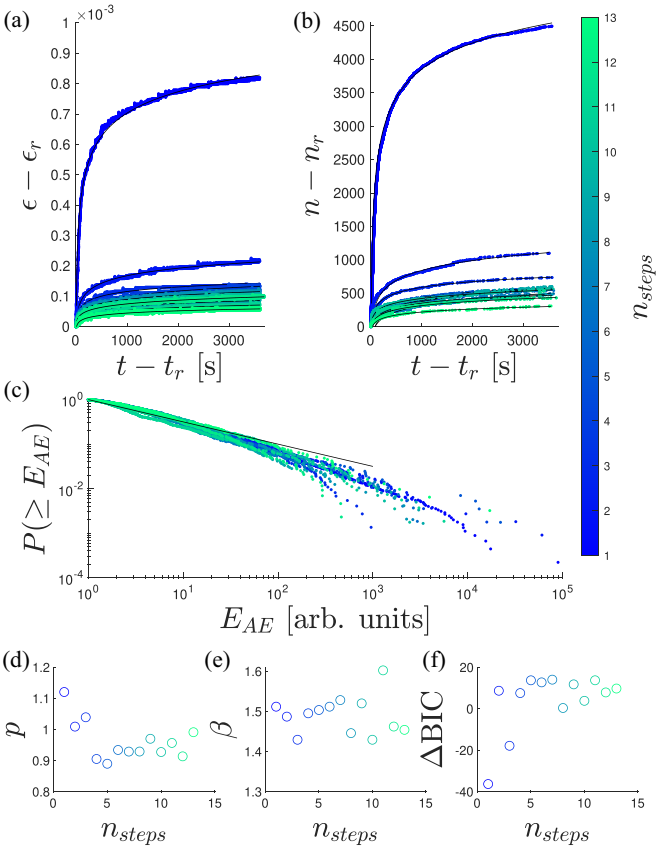

FIG. 4. A reference experiment with C-concrete where all the steps are performed at the same stress level (equal durations, unloading between steps). (a) The creep rates decrease quickly with increasing number of steps, and after around four steps the difference between steps becomes very hard to see. The black lines are fits corresponding to Eq. (1). (b) The number of acoustic events follows the behavior of strain in a linear fashion. The black lines are linear transformations of fits shown in panel (a). (c) The cumulative distribution of AE event energies shows a power-law distribution spanning several orders of magnitude for each creep step. The black line corresponds to $\beta = 3/2$. (d) The exponent p of the strain fits starts at a value $p \sim 1$ for the first steps (corresponding to logarithmic creep) and quickly decreases to a lower roughly constant value $p < 1$. (e) The energy distribution power-law exponent β is roughly constant, around the mean field value $\beta = 3/2$. The increased variance in the latter steps is due to the reduced number of events in these steps. (f) The difference of the BICs for the power-law and truncated power-law models in the energy distribution fits shows that the truncated power law is preferred only for the first and third steps.

of each creep step is significantly larger than in the end of the previous steps, showing effectively a restarting of the primary creep stage. Once again the number of acoustic events [Fig. 4(b)] follows from the relation $\dot{n} \propto \dot{\epsilon}$ and we see a robust power-law spanning several decades in energy [Fig. 4(c)]. The exponent p [Eq. (1)] of the strain curves [Fig. 4(d)] shows a slightly different behavior than in the other experiments (see Appendix B), the exponent is high in the first steps ($p \sim 1$ or even slightly larger) and decreases to a roughly constant value ($p < 1$) for the latter steps. The power-law exponent β fitted to the energy distributions [Fig. 4(e)] behaves as in the other

experiments, it is around 3/2 and does not evolve with the number of steps.

We also compute the difference in the Bayesian information criterions (BIC) [62,63] for the pure power-law distribution and a truncated one for the AE event energies. This quantity is negative if the observed data fit the truncated distribution better (for details see Appendix E). The difference in the BICs in the reference experiment [Fig. 4(f)] shows that the truncated power law is preferred only in the first and third steps and there is no clear cutoff in the acoustic emission energy distributions of the other steps. Even in the two cases where the truncated power law is preferred, it is associated to a fairly high cutoff value, $E_0 \sim 10^4$ arbitrary units.

V. SUMMARY

We studied primary creep of an emblematic heterogeneous material—concrete—under uniaxial compression. We observed a power-law (Omori-type) decrease in the strain rate and a similar behavior in the number of acoustic events, supporting the viewpoint of microcracking as the mechanism of creep deformation. This brittle creep mechanism, different from the microscopic mechanisms generally invoked to explain concrete creep, is further confirmed by our results of ultrasonic monitoring that show a similar evolution of the attenuation of elastic waves within the material as creep proceeds. It results from the interplay between thermal activation and elastic interactions leading to damage avalanches. Unlike what is observed for damage under athermal monotonic loading [47,48], the distribution of AE energies during primary creep follows a pure power law with an exponent close to the mean-field value even at low stress and quite far from failure, reminiscent of self-organized or extended criticality. The mechanism of this difference remains elusive, as the scale-free nature of the phenomena makes the pinpointing of a specific process difficult. Interestingly, this is reminiscent of the postseismic slip phase following large earthquakes, which is characterized by a power-law decrease of the slip velocity, $v \sim 1/(t+c)^p$ [64], as well as a similar decay of the aftershock triggering rate, the celebrated Omori's law [65], while the seismic moments of these aftershocks are distributed according to a nontruncated power law—the Gutenberg-Richter law [66].

However, the main outcome of this work is the discovery of loading history effects leading to an unexpected slowing down of primary creep dynamics after the material has been previously damaged during former creep steps. From a progressive damage model in which thermal activation of local damage events is introduced using a KMC algorithm, we argue that this results from an aging-under-stress phenomenon. In amorphous materials such as glasses, aging characterizes the process by which a glass, below its transition temperature, tries (very) slowly to reach thermal equilibrium by moving toward more stable energy wells [67]. This aging therefore modifies the excitation spectrum, increasing, on mechanically loading the amorphous material, its strength and brittleness [68]. In our case, the material ages during primary creep, i.e., under stress, assisted by thermal activation (as illustrated by the expression of the Arrhenius term $V_a \Delta\sigma_i / k_B T$ in the model). This depletes the easy-to-damage sites (smallest stress gaps), making the material less prone to creep when subsequently loaded under the same or even a *larger* stress. On increasing further the applied stress, one reaches finally a point at which this aging effect is counterbalanced by an increasing softening of the material and by elastic interactions leading to a sustained damage avalanche activity and larger creep rates. For a given primary creep step, this aging is fast at the onset of loading but slows down through time as creep proceeds (Fig. 2), much like classical aging of glasses [67].

The previously suggested phenomenological concepts of time or strain hardening [14–18] in creep suggest that the creep strain rate is only a function of the stress, temperature, and time (time hardening) or strain (strain hardening). Our results show a more complex behavior where the resultant strain from multiple stress steps cannot be expressed using a simple superposition principle as suggested by time hardening. As strain hardening in a brittle material such as concrete is negligible (compared to metals and plastics), it is not sufficient to explain our results. Our *aging under stress* scenario, with the modification of the excitation spectrum during primary creep as the easy-to-damage sites are exhausted, gives a theoretical explanation for these observed loading history effects.

Besides their importance for the fundamental understanding of creep in disordered brittle materials, these history effects have practical consequences in material testing that cannot be underestimated, e.g., when using stress-stepping experiments to empirically determine a creep law. Neglecting the aging-under-stress can falsely make the material seem more creep resistant than it actually is, which is a serious problem for structural materials.

Further work should be done to explore the observed history effects with much better statistics and to determine the influence of, e.g., creep step duration, stress step size, and temperature. Additionally, the impact of the history effects on the athermal failure strength or the creep failure time should be studied. Theoretical development of models explaining the scale-free power-law distributions of AE event energies instead of truncated ones is needed. Beyond brittle creep, one might expect similar aging-under-stress phenomena in other contexts, as already hinted at by Cottrell for the creep of metals [13]. In that case, creep results from dislocation motion, and this aging would result from the exhaustion of easy-to-deform sites during primary creep, resulting in a sort of statistical strain hardening. As the behavior can be modeled with a fairly general model of brittle materials, an extension to other materials, such as amorphous media, would be worth exploring as well.

ACKNOWLEDGMENTS

We thank Chi-Cong Vu for the sample preparation, Philémon Peltier for the implementation of the KMC algorithm, and Mikko Alava and Carmen Miguel for useful discussions. ISTerre is part of Labex OSUG@2020. T.M. acknowledges funding from the European Union Horizon 2020 research and innovation program under Grant No. 857470 and from European Regional Development Fund via Foundation for Polish Science International Research Agenda PLUS program Grant No. MAB PLUS/2018/8. The Aalto Science IT project is acknowledged for computational resources.

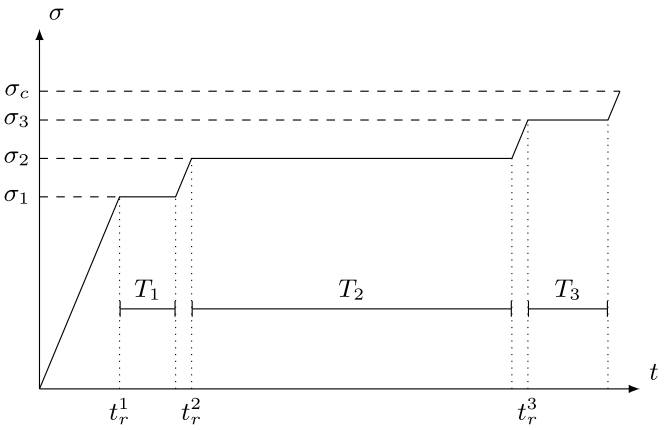

FIG. 5. A schematic picture of the loading protocol used. After an initial ramp of constant stress rate (ending at time t_r^1) the stress is kept constant at σ_1 for a duration T_1. The stress is then increased with the same stress rate to σ_2 for a duration of T_2 and so forth. The test ends when the sample fails either during a creep step (stress step) or during one of the ramps (at the stress σ_c).

APPENDIX A: DETAILS OF THE EXPERIMENTAL SETUP

The testing protocol comprises an initial loading ramp, static loading at constant stress σ_1 for a duration T_1, another loading ramp to σ_2, constant stress σ_2 for a duration T_2, and so forth until sample failure. A schematic representation of the loading protocol can be seen in Fig. 5, and the stresses and durations used for each creep step of each experiment are detailed in Table I. Experiment number 5 differs from the others, as there is an unloading ramp (identical to the initial loading ramp), a 15-min wait, and then a reloading ramp (again identical to the initial one) between each creep step. Due to the low stress used, this experiment was not performed until sample failure.

The samples used were cylindrical pieces of dry concrete with a radius of 40 mm and height of 80.5 ± 0.5 mm. Three sides of the samples were cut flat for imaging purposes (see Fig. 6(a) for a schematic representation) but the results of this imaging are not included in this paper. The loading direction during compression was perpendicular to the direction of casting. The two types of concrete used correspond to aggregate sizes of roughly 2 mm (M-concrete) and 3.5 mm (C-concrete) [52].

The cement used was CEM I 52.5N-type Portland cement, satisfying the standard NF EN 197-1 [69] and the aggregates were clean natural gravel, its specific properties conforming to the standard NF EN 12620 [70]. Ordinary potable water was used for mixing and curing, and the weight method (according to standard NF EN 206-1 [71]) was applied to prepare the concrete mixtures. The volume fraction of the aggregates was a constant 70% of the concrete volume and the finesse modulus of aggregates was 6.95 for M-concrete and 9.21 for C-concrete. The water-to-cement ratio was also a constant 58%.

The concrete samples were cast according to normal weight concrete procedure (standard NF EN 206-1 [71]) and during mixing the cement and aggregates were initially mixed in dry conditions and water was then added in the mixer. The mixtures were poured into cylindrical cardboard molds and the consolidation of the samples was improved by compacting them by an internal vibrator combined with an external vibrating table.

After casting the samples were cured for 48 h by covering the molds with a plastic sheet in a moisture room. After demolding, the specimens were cured in a water basin at a temperature of 20 °C for 2 months. The samples were then cut by diamond grinding disks to avoid flexural stresses and to ensure planar surfaces. After cutting the samples were stored in the water basin for an additional month and then stored in air-dried condition for 17 months. For experiment number 5 the sample had been stored in air-dried condition for 51 months.

The sample preparation and detailed microstructural analysis of the samples is detailed in Refs. [52,72].

TABLE I. Experimental details for all the experiments presented in the paper. Samples number 1 and 5 refer to the ones in the main text and the additional ones are presented in Appendix F.

Number	Type	σ_c (MPa)	Step	σ (MPa)	σ/σ_c	T (s)	n_{AE}
1	M	49.0	1	25.0	0.51	9199	8839
			2	30.0	0.61	12161	3877
			3	35.0	0.71	5976	1025
			4	40.0	0.82	7436	3914
			5	45.0	0.92	6225	5928
2	C	45.5	1	25.0	0.55	6982	787
			2	30.0	0.66	56630	1215
			3	35.0	0.77	10320	683
3	M	63.9	1	25.0	0.39	64040	3710
			2	30.0	0.47	1605	334
			3	35.0	0.55	1657	573
			4	40.0	0.63	1776	555
			5	45.0	0.70	940	496
			6	50.0	0.78	900	681
			7	55.0	0.86	838	1228
			8	60.0	0.94	911	4133
4	M	69.0	1	25.0	0.36	782	968
			2	30.0	0.44	782	667
			3	35.0	0.51	784	1127
			4	40.0	0.58	781	795
			5	45.0	0.65	782	752
			6	50.0	0.73	783	1272
			7	55.0	0.80	783	899
			8	60.0	0.87	782	1323
5	C		1	20.0		3595	4496
			2	20.0		3597	1099
			3	20.0		3596	736
			4	20.0		3599	561
			5	20.0		3599	569
			6	20.0		3599	541
			7	20.0		3599	494
			8	20.0		3599	482
			9	20.0		3599	601
			10	20.0		3617	566
			11	20.0		3598	539
			12	20.0		3685	432
			13	20.0		3607	310

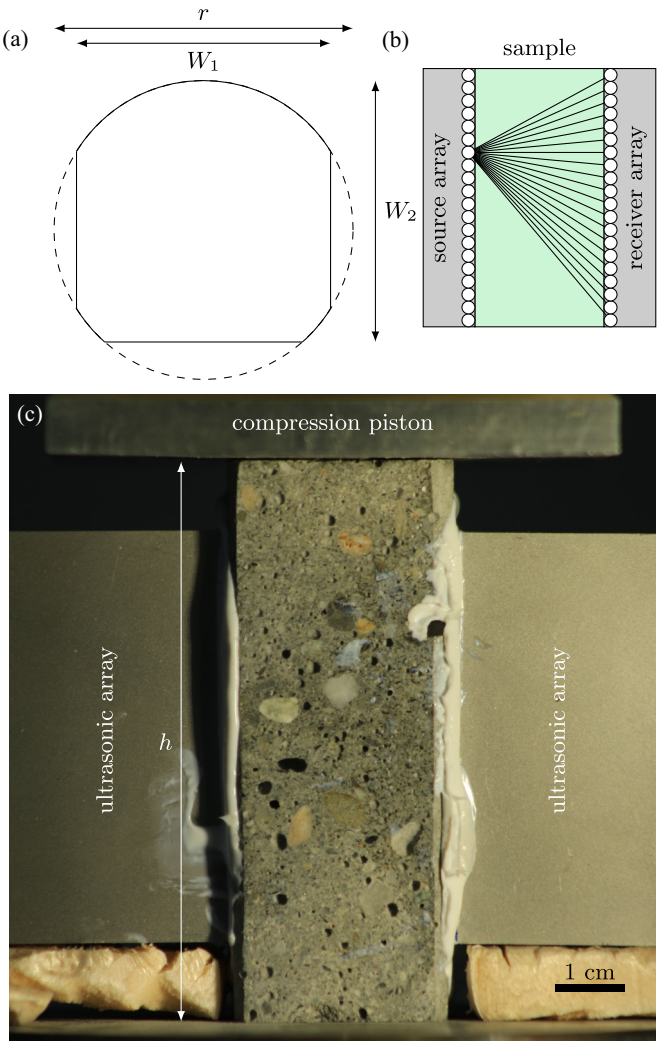

FIG. 6. (a) The geometry of the sample cross section showing the initially cylindrical samples (radius r) and the three flattened sides. (b) Schematic illustration of the operating principle of the ultrasonic array, showing the sample between the source and receiver arrays, where the white dots represent individual transducers (for clarity an array with 20 transducers is drawn). The black lines represent the direct path from one source transducer to each receiver transducers. (c) An image of the sample in the compression setup, showing the attachment of the ultrasonic arrays, as well as the heterogeneity of the sample microstructure. The height of the sample is denoted in the image as h.

The acoustic emission was captured by coupling two piezoelectric AE sensors (frequency bandwidth of 20–1200 kHz) directly to the side of the sample using a silicon paste. The resulting signals were preamplified by 40 dB and a standard thresholding procedure for AE event detection was used with a 30-dB amplitude threshold. The event catalog consists of the occurrence times of the events and their energies E_{AE}. The number of acoustic events during each creep step is detailed in Table I.

In addition, two source-receiver ultrasonic arrays face each other on both sides of the sample [Figs. 6(b) and 6(c)]. In ultrasonic monitoring, a pulse is sent from a source transducer and received in each of the receiver transducers, and this procedure is repeated for each transducer in the source array. The arrays are composed of 64 transducers centered at 1 MHz with a 75% bandwidth. The ultrasonic signal transmitted by each piezotransducer source is a broadband pulse of 1 μs at the central frequency of the transducer. On both arrays, the transducer dimensions are 0.75 mm along the vertical axis (that corresponds to half of the central wavelength) and 12 mm along the transverse axis. This feature naturally creates a collimated beam, which avoids side echoes from the sample boundaries. The received signals spread over 10 μs after the direct arrival at $\simeq$9 μs due to weak scattering associated to the sample heterogeneity. To solely focus on the amplitude variation of the ballistic arrival, a double beamforming algorithm (DBF) is applied on subarrays of nine elements centered on source-receiver pairs from both sides [53]. The DBF algorithm presents two advantages. First, it allows us to clean out the scattered wavefield with the selection of the acoustic beam of maximum intensity for each source-receiver pair [73]. Second, it significantly improves the signal-to-noise ratio of the ballistic arrival when the elastic attenuation increases close to failure [74]. The averaging of the amplitudes is done over all of these beams, i.e., over the whole sample.

APPENDIX B: DETAILS OF THE SIMULATION MODEL

The basic framework of the model is a well-studied progressive damage model [54–56] that utilizes a two-dimensional plane strain finite element method with a triangular mesh and adds the damage through a decrease in the elastic modulus,

$$E = (1 - d)E_0, \tag{B1}$$

where E_0 is the initial elastic modulus and d the damage parameter. Each time an element is damaged (the criterion for this is explained below) the modulus is decreased by 10%, which is merely an arbitrary choice for the damage parameter and does not change the general behavior of the model.

The time-dependent part is implemented using the KMC approach which works in two basic steps. First, a site is picked randomly, with a probability proportional to the jump rate which follows an activated scaling,

$$\nu_i = \nu_0 \exp\left(-\frac{E_i}{k_B T}\right), \tag{B2}$$

where the index i corresponds to the site in the simulated sample, ν_0 is the constant attempt frequency, E the activation energy, k_B the Boltzmann constant, and T the absolute temperature. The activation energy is determined as $E_i = V\Delta\sigma_i$, where V is a (constant) activation volume and $\Delta\sigma$ is the size of the stress step in the Coulomb failure criterion at the current time (Fig. 7).

After the site is picked, it is damaged according to the original formulation of the model. The second step of the KMC algorithm is then a random choice of the time step from a distribution with the probability density function

$$p(\Delta t) = \frac{1}{\Delta t_0} \exp\left(-\frac{\Delta t}{\Delta t_0}\right), \tag{B3}$$

where Δt_0 is the reciprocal of the sum of the jump rates $\sum_i \nu_i$. The simulation time used is moved forward by this

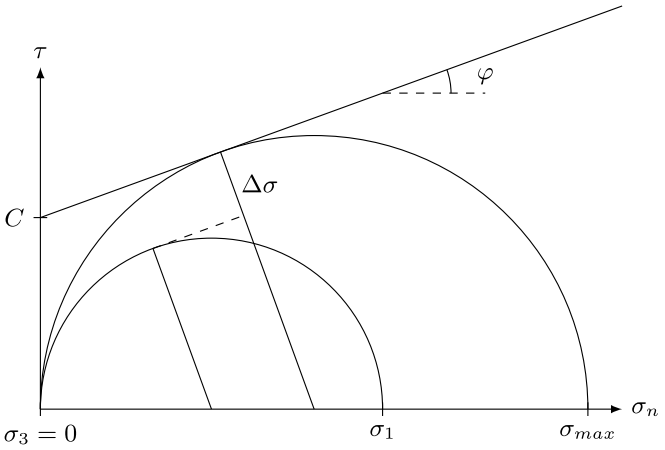

FIG. 7. An illustration of the Coulomb failure criterion used, represented in the Mohr plane. The stress gap $\Delta\sigma$ is defined as the distance from the current stress state (circle defined by the applied normal stress σ_1) to the failure envelope (defined by the line with a slope $\tan\varphi$ and y intercept C).

randomly chosen Δt and the cycle starts again from the first step. We note that the simulation timescale is inversely proportional to ν_0, and the exact time values used in this work rely on this fairly arbitrarily chosen parameter. The value is an order-of-magnitude estimate based on the activation energy for subcritical crack growth in rocks [75].

The stress step used in the model is determined from the classical Coulomb failure criterion. The critical normal stress $\sigma_{\max}$ is determined by the envelope

$$\tau = C_i + \sigma_n \tan\varphi, \tag{B4}$$

where τ is the shear strength, C_i the cohesion value of the site, σ_n the normal stress, and φ the angle of internal friction. The cohesion values for each site are picked from a quenched uniform distribution spanning from 0 to $C_{\max}$.

The stress gap $\Delta\sigma$ is then the distance from the current state to the athermal failure state (see Fig. 7 for a graphical explanation). Here only normal stress is applied and therefore $\sigma_n = \sigma_1$ and the stress gap is

$$\Delta\sigma = C\cos\varphi + \frac{\sigma_1 + \sigma_3}{2}\sin\varphi - \frac{\sigma_1 - \sigma_3}{2}. \tag{B5}$$

The values of the model parameters chosen to mimic the macroscopic behavior observed experimentally can be seen in Table II.

TABLE II. Parameter values for the model

E_0 (GPa)	d	ν_0 (s^{-1})	T (K)
21	0.1	1×10^{13}	300
V (m^3)	φ (°)	$C_{\max}$ (MPa)	
11×10^{-27}	35	31	

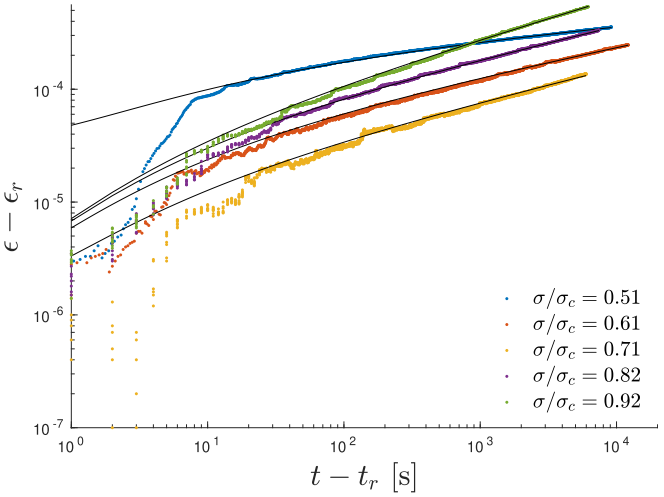

FIG. 8. Figure 1(a) with double logarithmic axes.

APPENDIX C: GOODNESS-OF-FIT ANALYSIS FOR THE STRAIN EVOLUTION

To illustrate the goodness-of-fit for the strain fits presented in Fig. 1(a) of the main text [fits to Eq. (1) of the main text], we plot them here in double logarithmic axes in Fig. 8. The fits are extremely good on timescales over 10 s. Below this there is a fair bit of disparity between the fits and the measured strain values. We, however, note that the actual strain differences even on timescales less than 10 s are extremely small.

Another way to illustrate the goodness-of-fit is to plot the residuals of the fitting, which are just the absolute differences between the fitted strain values ϵ_{fit} and the measured strains

$$|\epsilon_{\text{fit}} - \epsilon| = \left|\epsilon_0 + \int_0^t \frac{K}{(t' - t_r + c)^p} dt' - \epsilon\right|, \tag{C1}$$

where ϵ_0 is the initial strain value used while fitting the integral of the strain rate relation presented in Eq. (1). These residuals are illustrated in Fig. 9, where we see that except for the first 10 s of the first creep step the residuals are below 10^{-5}.

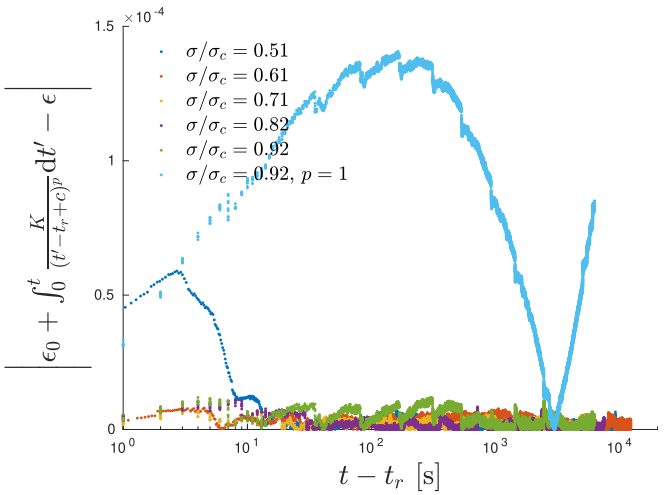

FIG. 9. Residuals of the fits shown in Fig. 1(a), and an additional one where Eq. (1) is fitted to the last creep step with fixed $p = 1$.

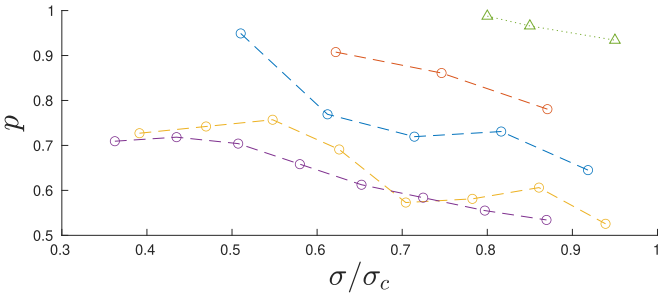

FIG. 10. The evolution of the p exponent in Eq. (1) as a function of the scaled applied stress. The triangle symbols correspond to the simulations and the circles to the experiments.

Additionally, we compare our fits to a fit assuming logarithmic creep [Eq. (1) with $p = 1$] for one of the creep steps. We clearly see from Fig. 9 that the residual of the fit is much greater than for our fits with $p < 1$. We can thus exclude logarithmic creep when we clearly see an exponent $p < 1$.

APPENDIX D: EVOLUTION OF THE *P*-EXPONENT VALUES

In the main text we state that fitting the strain rate relation [Eq. (1)] to the observed strain curves [Fig. 1(a)] shows that the exponent p decreases with increasing stress. This effect is shown in Fig. 10 where p is plotted as a function of the scaled applied stress σ/σ_c. The decrease is clear in all the experiments (plotted with circles) although the initial value of the exponent varies from around 0.7 to almost unity. The same behavior is seen in the simulations (plotted with triangles) where the initial value of p is very close to unity and decreases with increasing stress. The decrease is roughly linear in all cases (slope of a linear fit -0.46 ± 0.11) and the duration of the creep step does not seem to have a strong effect on the decrease.

APPENDIX E: STATISTICAL ANALYSIS OF THE ACOUSTIC EMISSION

From the dataset of N events with energies E^i_{AE} (where $i \in [1, N]$) the parameters of the event energy distribution are estimated using the maximum likelihood method [76] where one computes the (logarithm of the) likelihood function $\mathcal{L}$ and finds the parameters which maximize this function.

The natural choices for the distributions we see are a power law (PL),

$$p(E_{\mathrm{AE}}) = \frac{E_{\mathrm{AE}}^{-\beta}}{\zeta_{\mathrm{PL}}}, \tag{E1}$$

where ζ_{PL} is the normalization factor and the truncated power law (TPL) or power law with an exponential cutof,f

$$p(E_{\mathrm{AE}}) = \frac{E_{\mathrm{AE}}^{-\beta}\exp(-E_{\mathrm{AE}}/E_0)}{\zeta_{\mathrm{TPL}}}, \tag{E2}$$

which give the log-likelihoods

$$\ln \mathcal{L}_{\mathrm{PL}} = -\beta \sum_{i=1}^{N} \ln E^i_{\mathrm{AE}} - N \ln \zeta_{\mathrm{PL}} \tag{E3}$$

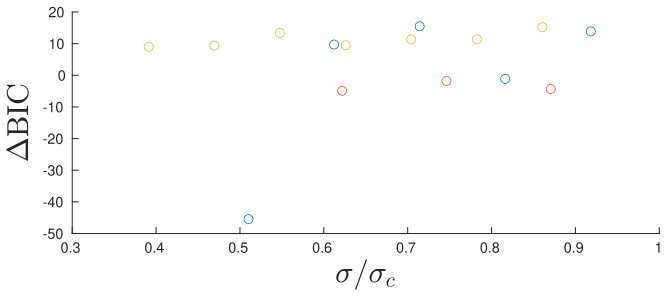

FIG. 11. The evolution of the difference of the BICs for the power-law and truncated power-law models [Eq. (E6)] in the experiments as a function of the scaled applied stress, showing that the truncated power law is significantly favored in only one of the stress steps.

and

$$\ln \mathcal{L}_{\mathrm{TPL}} = -\beta \sum_{i=1}^{N} \ln E^i_{\mathrm{AE}} + \sum_{i=1}^{N} \frac{E^i_{\mathrm{AE}}}{E_0} - N \ln \zeta_{\mathrm{TPL}}. \tag{E4}$$

As the two models have a different number of parameters, a direct comparison of the likelihoods is not the best way to compare their goodness-of-fit. Instead, for comparison one can compute the BIC [62,63],

$$\mathrm{BIC} = -2 \ln \mathcal{L} + 2N_p \ln N, \tag{E5}$$

where N_p is the number of parameters. The more illustrative quantity is the difference of the BICs for the power-law and truncated power-law models,

$$\Delta\mathrm{BIC} = 2(\ln \mathcal{L}_{\mathrm{PL}} - \ln \mathcal{L}_{\mathrm{TPL}} - \ln N), \tag{E6}$$

which is negative if the truncated power law is favored, positive if the pure power law is favored, and around zero if the models give equally good results.

Plotting the ΔBIC as a function of the scaled applied stress [Figs. 4(f) and 11] shows that it is generally positive or fairly close to zero for almost every stress step in the experiments.

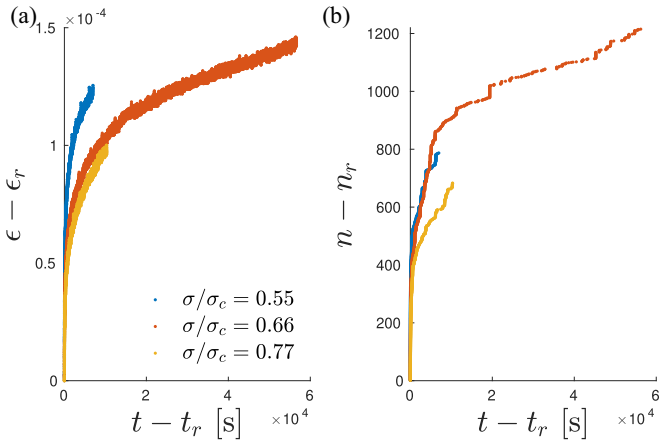

FIG. 12. An additional experiment (number 2) with C-concrete showing that the behavior with this microstructure is very similar to the M-concrete. (a) After an initial stress step the creep is slower and as the second step is fairly long, the creep is even slower in the third step. (b) The number of acoustic events shows behavior which is very similar to the time evolution of the strain.

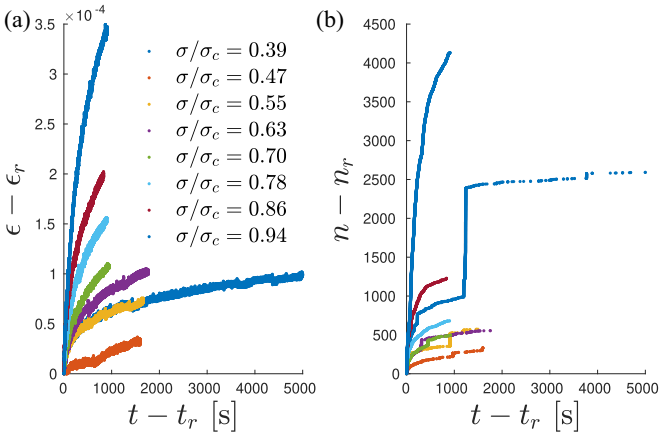

FIG. 13. An additional experiment (number 3) with M-concrete, showing the effect of an extremely long initial stress step (real duration 64 036 s, plot truncated for clarity) on subsequent, short stress steps. (a) After the extremely long initial step the next (fairly short) step shows very slow creep and in the third step the creep rate is only roughly equal to the first one. (b) Except for one sudden burst of events in the first stress step, the number of acoustic events roughly follows the behavior of the strain.

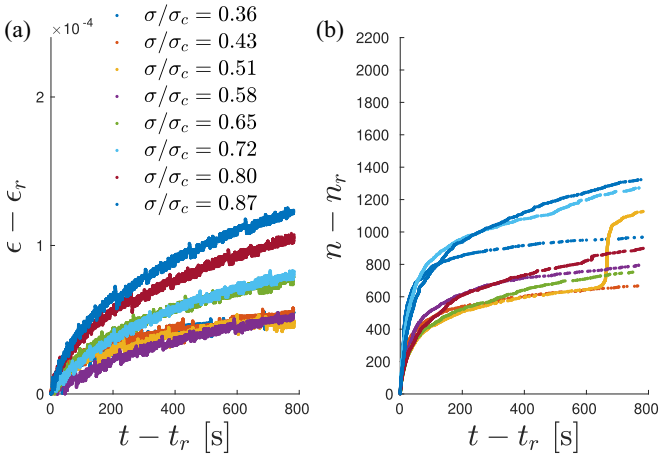

FIG. 14. A reference experiment (number 4) with M-concrete where all the stress steps are kept short (equal durations). (a) The creep rates for the first three steps are roughly equal and after that start to increase. This behavior is not consistent with the power-law model $\dot{\epsilon} \propto \sigma^n$. (b) Also here the behavior of the number of acoustic events roughly matches the behavior of strain. There is again a sudden burst of events close to the end of one stress step.

This is expected, as with a high cutoff value the power law and truncated power law should yield similarly good fits. However, for a few stress steps (some initial steps in the experiments presented in the main text) the truncated power law is clearly preferred, but also here the cutoff value is fairly high, around $E_0 \sim 10^4$ arbitrary units. Even in the cases where the truncated power law is preferred, the behavior clearly differs from the diverging cutoff scale observed previously for monotonic loading of concrete [47].

APPENDIX F: ADDITIONAL EXPERIMENTS

For the sake of clarity, only one representative experiment, as well as a reference one, are presented in the main text, but several other experiments were performed, with varying durations of stress steps as well as microstructures. We have included the strain and event count behaviors of these experiments in Figs. 12–14. History effects similar to those analyzed for the representative experiment detailed in the main text are observed in each case for both the strain and the number of AE events.

In addition to exploring varying creep step durations and microstructures we also performed an additional reference experiment (number 4, Fig. 14) where the step durations were kept equal and short to minimize the history effect. What we observe is roughly equal creep rates for the first three steps, which is not consistent with the power-law model $\dot{\epsilon} \propto \sigma^n$. After these steps—as the sample failure is approached—the creep rate starts to increase, as expected based on our other results.

[1] N. L. Carter and S. H. Kirby, Transient creep and semibrittle behavior of crystalline rocks, in *Rock Friction and Earthquake Prediction*, edited by J. D. Byerlee and M. Wyss (Birkhäuser, Basel, 1978), pp. 807–839.

[2] J. Weiss and D. Amitrano, Logarithmic vs Andrade's transient creep: The role of elastic stress redistribution, arXiv:2206.06682 (2022).

[3] E. N. D. C. Andrade, On the viscous flow in metals, and allied phenomena, Proc. Roy. Soc. Lond. Ser. A **84**, 1 (1910).

[4] A. Cottrell, Logarithmic and Andrade creep, Philos. Mag. Lett. **75**, 301 (1997).

[5] H. Nechad, A. Helmstetter, R. El Guerjouma, and D. Sornette, Creep Ruptures in Heterogeneous Materials, Phys. Rev. Lett. **94**, 045501 (2005).

[6] M. Leocmach, C. Perge, T. Divoux, and S. Manneville, Creep and Fracture of a Protein Gel Under Stress, Phys. Rev. Lett. **113**, 038303 (2014).

[7] J. Koivisto, M. Ovaska, A. Miksic, L. Laurson, and M. J. Alava, Predicting sample lifetimes in creep fracture of heterogeneous materials, Phys. Rev. E **94**, 023002 (2016).

[8] T. Mäkinen, J. Koivisto, L. Laurson, and M. J. Alava, Scale-free features of temporal localization of deformation in late stages of creep failure, Phys. Rev. Mater. **4**, 093606 (2020).

[9] M. F. Ashby and D. R. Jones, *Engineering Materials 1: An Introduction to Properties, Applications and Design*, Vol. 1 (Elsevier, Amsterdam, 2012).

[10] M. Heap, P. Baud, P. Meredith, A. Bell, and I. Main, Time-dependent brittle creep in Darley Dale sandstone, J. Geophys. Res.: Solid Earth **114**, B07203 (2009).

[11] N. Brantut, M. Heap, P. Meredith, and P. Baud, Time-dependent cracking and brittle creep in crustal rocks: A review, J. Struct. Geol. **52**, 17 (2013).

[12] Z. Geng, A. Bonnelye, M. Chen, Y. Jin, P. Dick, C. David, X. Fang, and A. Schubnel, Time and temperature dependent creep

in Tournemire shale, J. Geophys. Res.: Solid Earth **123**, 9658 (2018).
[13] A. Cottrell, The time laws of creep, J. Mech. Phys. Solids **1**, 53 (1952).
[14] C. Davenport, Correlation of creep and relaxation properties of copper, J. Appl. Mech. **5**, A55 (1938).
[15] G. E. Lucas and R. Pelloux, Some observations on time-hardening and strain-hardening rules for creep in Zircaloy-2, Nucl. Technol. **53**, 46 (1981).
[16] N. Ogbonna, N. Fleck, and A. Cocks, Transient creep analysis of ball indentation, Int. J. Mech. Sci. **37**, 1179 (1995).
[17] W. N. Findley and G. Khosla, Application of the superposition principle and theories of mechanical equation of state, strain, and time hardening to creep of plastics under changing loads, J. Appl. Phys. **26**, 821 (1955).
[18] P. C. Roozemond, V. Janssens, P. Van Puyvelde, and G. W. Peters, Suspension-like hardening behavior of HDPE and time-hardening superposition, Rheol. Acta **51**, 97 (2012).
[19] M. Siebenbürger, M. Ballauff, and T. Voigtmann, Creep in Colloidal Glasses, Phys. Rev. Lett. **108**, 255701 (2012).
[20] T. Divoux, C. Barentin, and S. Manneville, From stress-induced fluidization processes to Herschel-Bulkley behaviour in simple yield stress fluids, Soft Matter **7**, 8409 (2011).
[21] P. Lidon, L. Villa, and S. Manneville, A mesoscale study of creep in a microgel using the acoustic radiation force, Soft Matter **15**, 2688 (2019).
[22] J. W. Glen, The creep of polycrystalline ice, Proc. R. Soc. Lond. A **228**, 519 (1955).
[23] C. Scholz, Mechanism of creep in brittle rock, J. Geophys. Res. **73**, 3295 (1968).
[24] N. Mott, A theory of work-hardening of metals II: Flow without slip-lines, recovery and creep, Lond. Edinb. Dubl. Philos. Mag. J. Sci. **44**, 742 (1953).
[25] A. Cottrell, A microscopic theory of Andrade creep, Philos. Mag. Lett. **84**, 685 (2004).
[26] F. Louchet and P. Duval, Andrade creep revisited, Int. J. Mater. Res. **100**, 1433 (2009).
[27] M.-Carmen Miguel, A. Vespignani, M. Zaiser, and S. Zapperi, Dislocation Jamming and Andrade Creep, Phys. Rev. Lett. **89**, 165501 (2002).
[28] F. H. Wittmann, Creep and shrinkage mechanisms, in *Creep and Shrinkage in Concrete Structures*, edited by Z. P. Bazant and F. H. Wittmann (Wiley, New York, 1982), pp. 129–161.
[29] F. Benboudjema, F. Meftah, and J.-M. Torrenti, Interaction between drying, shrinkage, creep and cracking phenomena in concrete, Eng. Struct. **27**, 239 (2005).
[30] M. Vandamme and F.-J. Ulm, Nanogranular origin of concrete creep, Proc. Natl. Acad. Sci. USA **106**, 10552 (2009).
[31] H. Manzano, E. Masoero, I. Lopez-Arbeloa, and H. M. Jennings, Shear deformations in calcium silicate hydrates, Soft Matter **9**, 7333 (2013).
[32] A. Morshedifard, S. Masoumi, and M. Abdolhosseini Qomi, Nanoscale origins of creep in calcium silicate hydrates, Nat. Commun. **9**, 1785 (2018).
[33] M. Haist, T. Divoux, K. J. Krakowiak, J. Skibsted, Roland J.-M. Pellenq, H. S. Müller, and F.-J. Ulm, Creep in reactive colloidal gels: A nanomechanical study of cement hydrates, Phys. Rev. Res. **3**, 043127 (2021).
[34] Z. P. Bažant and J. Planas, *Fracture and Size Effect in Concrete and Other Quasibrittle Materials* (CRC Press, Boca Raton, 1998).
[35] M. Briffaut, F. Benboudjema, J.-M. Torrenti, and G. Nahas, Concrete early age basic creep: Experiments and test of rheological modelling approaches, Construct. Build. Mater. **36**, 373 (2012).
[36] A. Hilaire, F. Benboudjema, A. Darquennes, Y. Berthaud, and G. Nahas, Modeling basic creep in concrete at early-age under compressive and tensile loading, Nucl. Eng. Des. **269**, 222 (2014).
[37] A. Sellier, S. Multon, L. Buffo-Lacarrière, T. Vidal, X. Bourbon, and G. Camps, Concrete creep modelling for structural applications: Non-linearity, multi-axiality, hydration, temperature and drying effects, Cement Concr. Res. **79**, 301 (2016).
[38] A. B. Giorla and C. F. Dunant, Microstructural effects in the simulation of creep of concrete, Cement Concr. Res. **105**, 44 (2018).
[39] Y. Geng, M. Zhao, H. Yang, and Y. Wang, Creep model of concrete with recycled coarse and fine aggregates that accounts for creep development trend difference between recycled and natural aggregate concrete, Cement Concr. Compos. **103**, 303 (2019).
[40] J. P. Sethna, K. A. Dahmen, and C. R. Myers, Crackling noise, Nature **410**, 242 (2001).
[41] J. Baró, Á. Corral, X. Illa, A. Planes, E. K. H. Salje, W. Schranz, D. E. Soto-Parra, and E. Vives, Statistical Similarity Between the Compression of a Porous Material and Earthquakes, Phys. Rev. Lett. **110**, 088702 (2013).
[42] D. Lockner, The role of acoustic emission in the study of rock fracture, in *International Journal of Rock Mechanics and Mining Sciences & Geomechanics Abstracts*, Vol. 30 (Elsevier, Amsterdam, 1993), pp. 883–899.
[43] J. Davidsen, S. Stanchits, and G. Dresen, Scaling and Universality in Rock Fracture, Phys. Rev. Lett. **98**, 125502 (2007).
[44] T. Mäkinen, J. Koivisto, E. Pääkkönen, J. A. Ketoja, and M. J. Alava, Crossover from mean-field compression to collective phenomena in low-density foam-formed fiber material, Soft Matter **16**, 6819 (2020).
[45] M. Reichler, S. Rabensteiner, L. Törnblom, S. Coffeng, L. Viitanen, L. Jannuzzi, T. Mäkinen, J. R. Mac Intyre, J. Koivisto, A. Puisto *et al.*, Scalable method for bio-based solid foams that mimic wood, Sci. Rep. **11**, 24306 (2021).
[46] T. Mäkinen, A. Miksic, M. Ovaska, and M. J. Alava, Avalanches in Wood Compression, Phys. Rev. Lett. **115**, 055501 (2015).
[47] C.-C. Vu, D. Amitrano, O. Plé, and J. Weiss, Compressive Failure as a Critical Transition: Experimental Evidence and Mapping onto The Universality Class of Depinning, Phys. Rev. Lett. **122**, 015502 (2019).
[48] C.-C. Vu and J. Weiss, Asymmetric Damage Avalanche Shape in Quasibrittle Materials and Subavalanche (Aftershock) Clusters, Phys. Rev. Lett. **125**, 105502 (2020).
[49] D. S. Fisher, Collective transport in random media: From superconductors to earthquakes, Phys. Rep. **301**, 113 (1998).
[50] K. A. Dahmen, Y. Ben-Zion, and J. T. Uhl, Micromechanical Model for Deformation in Solids with Universal Predictions for Stress-Strain Curves and Slip Avalanches, Phys. Rev. Lett. **102**, 175501 (2009).

[51] O. Narayan and D. S. Fisher, Threshold critical dynamics of driven interfaces in random media, Phys. Rev. B **48**, 7030 (1993).

[52] C.-C. Vu, Statistical size effects on compressive strength of concrete, Ph.D. thesis, Université Grenoble Alpes, 2018.

[53] E. Tudisco, P. Roux, S. A. Hall, G. M. Viggiani, and G. Viggiani, Timelapse ultrasonic tomography for measuring damage localization in geomechanics laboratory tests, J. Acoust. Soc. Am. **137**, 1389 (2015).

[54] D. Amitrano, J.-R. Grasso, and D. Hantz, From diffuse to localised damage through elastic interaction, Geophys. Res. Lett. **26**, 2109 (1999).

[55] L. Girard, D. Amitrano, and J. Weiss, Failure as a critical phenomenon in a progressive damage model, J. Stat. Mech.: Theory Exp. (2010) P01013.

[56] L. Girard, J. Weiss, and D. Amitrano, Damage-Cluster Distributions and Size Effect on Strength in Compressive Failure, Phys. Rev. Lett. **108**, 225502 (2012).

[57] A. F. Voter, Introduction to the kinetic Monte Carlo method, in *Radiation Effects in Solids* (Springer, Berlin, 2007), pp. 1–23.

[58] J. Lin, A. Saade, E. Lerner, A. Rosso, and M. Wyart, On the density of shear transformations in amorphous solids, Europhys. Lett. **105**, 26003 (2014).

[59] J. Lin, E. Lerner, A. Rosso, and M. Wyart, Scaling description of the yielding transition in soft amorphous solids at zero temperature, Proc. Natl. Acad. Sci. USA **111**, 14382 (2014).

[60] C. Liu, E. E. Ferrero, F. Puosi, J.-L. Barrat, and K. Martens, Driving Rate Dependence of Avalanche Statistics and Shapes at the Yielding Transition, Phys. Rev. Lett. **116**, 065501 (2016).

[61] M. Ovaska, A. Lehtinen, M. J. Alava, L. Laurson, and S. Zapperi, Excitation Spectra in Crystal Plasticity, Phys. Rev. Lett. **119**, 265501 (2017).

[62] A. F. Bell, M. Naylor, and I. G. Main, Convergence of the frequency-size distribution of global earthquakes, Geophys. Res. Lett. **40**, 2585 (2013).

[63] J. Vasseur, F. B. Wadsworth, Y. Lavallée, A. F. Bell, I. G. Main, and D. B. Dingwell, Heterogeneity: The key to failure forecasting, Sci. Rep. **5**, 13259 (2015).

[64] A. Periollat, M. Radiguet, J. Weiss, C. Twardzik, D. Amitrano, N. Cotte, L. Marill, and A. Socquet, Transient Brittle Creep mechanism explains early postseismic phase of the 2011 Tohoku-Oki megathrust earthquake: Observations by high-rates GPS solutions, J. Geophys. Res. **127**, JB024005 (2022).

[65] F. Omori, On the after-shocks of earthquakes, Ph.D. thesis, The University of Tokyo, 1895.

[66] Y. Y. Kagan, *Earthquakes: Models, Statistics, Testable Forecasts* (John Wiley & Sons, New York, 2013).

[67] F. Arceri, F. Landes, L. Berthier, and G. Biroli, A statistical mechanics perspective on glasses and aging, in *Encyclopedia of Complexity and Systems Science* (Springer, Berlin, 2021).

[68] M. Ozawa, L. Berthier, G. Biroli, A. Rosso, and G. Tarjus, Random critical point separates brittle and ductile yielding transitions in amorphous materials, Proc. Natl. Acad. Sci. USA **115**, 6656 (2018).

[69] NF EN 197-1, *Ciment – Partie 1: Compostition, Spécifications et Critères de Conformité Desciments Courants* (Association Française de Normalisation, Paris, 2012).

[70] NF EN 12620, *Granulats Pour Béton* (Association Française de Normalisation, Paris, 2008).

[71] NF EN 206-1, *Béton—Partie 1: Spécification, Performances, Production et Conformité* (Association Française de Normalisation, Paris, 2004).

[72] C.-C. Vu, J. Weiss, O. Ple, D. Amitrano, and D. Vandembroucq, Revisiting statistical size effects on compressive failure of heterogeneous materials, with a special focus on concrete, J. Mech. Phys. Solids **121**, 47 (2018).

[73] I. Iturbe, P. Roux, J. Virieux, and B. Nicolas, Travel-time sensitivity kernels versus diffraction patterns obtained through double beam-forming in shallow water, J. Acoust. Soc. Am. **126**, 713 (2009).

[74] B. Nicolas, I. Iturbe, P. Roux, and J. I. Mars, Double Beamforming for wave separation and identification: Robustness against noise and application on FAF03 experiment, Trait. Sign. **25**, 293 (2008), https://www.iieta.org/journals/ts/paper/10.3166/TS.25.293-304.

[75] B. K. Atkinson, Subcritical crack growth in geological materials, J. Geophys. Res.: Solid Earth **89**, 4077 (1984).

[76] J. Baró and E. Vives, Analysis of power-law exponents by maximum-likelihood maps, Phys. Rev. E **85**, 066121 (2012).